Mechatronics 23 (2013) 659–668

Contents lists available at ScienceDirect

Mechatronics

journal homepage: www.elsevier.com/locate/mechatronics

A dynamic model for tail-actuated robotic fish with drag coefficient adaptation ☆

Jianxun Wang, Xiaobo Tan *

Department of Electrical and Computer Engineering, Michigan State University, East Lansing, MI 48824, United States

ARTICLE INFO

Article history:
Received 19 January 2013
Accepted 1 July 2013
Available online 17 August 2013

Keywords:
Robotic fish
Dynamic model
Carangiform locomotion
Large-amplitude elongated-body theory
Experimental model validation
Drag coefficient adaptation

ABSTRACT

In this paper we present a dynamic model for a tail-actuated robotic fish by merging rigid-body dynamics with Lighthill's large-amplitude elongated-body theory. The model is validated with extensive experiments conducted on a robotic fish prototype. We investigate the role of incorporating the body motion in evaluating the tail-generated hydrodynamic force, and show that ignoring the body motion (as often done in the literature) results in significant overestimate of the thrust force and robot speed. By exploiting the strong correlation between the angle of attack and the tail-beat bias, a computationally efficient approach is further proposed to adapt the drag coefficients of the robotic fish, and its effectiveness is supported by experimental results.

1. Introduction

With five hundred million years of evolution, fish and other aquatic animals are endowed with a variety of morphological and structural features that enable them to move through water with speed, efficiency, and agility [1,2]. The remarkable feats in biological swimming have stimulated extensive theoretical [3–5], experimental [6–10], and computational [11,12] research by biologists, mathematicians, and engineers, in an effort to understand and mimic locomotion, maneuvering, and sensing mechanisms adopted by aquatic animals.

Over the past two decades, there has also been significant interest in developing underwater robots that propel and maneuver themselves like real fish do [13–34]. Often termed *robotic fish*, these robots provide an experimental platform for studying fish swimming, and hold strong promise for a number of underwater applications such as environmental monitoring [35]. Instead of using propellers, robotic fish accomplish swimming by deforming the body and/or fin-like appendages, mostly functioning as caudal fins and sometimes as pectoral fins. Body deformation and fin movements are typically achieved with motors. On the other hand, advances in smart materials have been explored to realize noiseless and compact actuation of robotic fish [28,29,36–43].

Carangiform locomotion, where movement is mainly restricted to the last third of the body length, is one of the most popular swimming modes observed in fish due to its sound balance between speed and maneuverability [7,44,45]. For this reason, carangiform has also been a prominent locomotion mode for reported robotic fish prototypes. In addition, this mode features a relatively big and rigid body that is ideal for housing electronics and sensors.

Dynamic modeling [5,20,24,28,29,31,46–53], trajectory planning, and control [18,24,54–59] of robotic fish have received extensive attention. A major challenge in the modeling of robotic fish lies in properly capturing the fluid–structure interactions and the resulting force and moment on the robot. While computational fluid dynamics (CFD) modeling [11,12,60,61] can provide high-fidelity representation of such interactions, it is not amenable to control design. A few alternatives are available. The first is to apply quasi-steady lift and drag models from airfoil theory to the body and fin surfaces of underwater robots [24,46,49,50]. Another approach is to assume perfect fluids (irrotational potential flow) and exploit the symmetry to obtain a finite-dimensional model [51,58], but some coefficients of such models may have to be obtained numerically [51]. Effects of vorticity can be accommodated by assuming, for example, vortices periodically shed from the tail fin [5,48].

The third approach to the evaluation of hydrodynamic forces is to use Lighthill's elongated-body theory [3]. This theory captures the reactive force between body and fluids with an added-mass effect, and it approximates the effect of wake dynamics by considering the momentum balance in a half-space control volume,

☆ This work was supported in part by NSF (CCF-0820220, DBI-0939454, IIS-0916720, ECCS-1050236, ECCS-1029683, CNS-1059373) and ONR (Grant N000140810640).

* Corresponding author. Tel.: +1 517 432 5671; fax: +1 517 353 1980.
E-mail addresses: wangji19@msu.edu (J. Wang), xbtan@egr.msu.edu (X. Tan).

0957-4158/$ - see front matter © 2013 Elsevier Ltd. All rights reserved.
http://dx.doi.org/10.1016/j.mechatronics.2013.07.005

which contains the deforming body and is bounded by a vertical plane attached to the trailing edge. Consequently, the resulting force and moment only depend on the configuration of the (robotic) fish. Lighthill's model strikes a sound balance between fidelity and simplicity, and its effectiveness in robotic fish modeling has been demonstrated in the prior work of one of the coauthors [28,62].

The contributions of this work are twofold. First, we present a dynamic model for a tail-actuated robotic fish by combining rigid-body dynamics with Lighthill's large-amplitude elongated-body theory, and validate the model with extensive experiments conducted on a robotic fish prototype. Specifically, we consider rigid-body dynamics for the robot body and adopt Lighthill's theory to capture the tail-actuation effect. To our best knowledge, such an approach has not been reported in the literature. Our prior work [28,62] involving Lighthill's theory was focused on steady-state motions, where the dynamics of the robot was not considered. Chen et al. applied a similar approach to evaluate the thrust produced by undulatory body motion of a robot tuna [63], but the analysis therein dealt with only *point-mass dynamics* for the robot, where forward-swimming was studied via simulation. Note that rigid body dynamics allows one to capture both body translation and rotation, and is significantly more complex and relevant than point-mass dynamics in terms of capturing the true behavior of the robot. Using the proposed model, we investigate the role of incorporating the body motion in evaluating the tail-produced hydrodynamic force, and show that ignoring the body motion (as often done in the literature [28,29,64]) results in significant overestimate of the thrust force and robot speed.

The second contribution of this work is a computationally efficient approach to the adaptation of drag coefficients for robotic fish. These coefficients play a significant role in the modeling of underwater vehicles and are often functions of the angle of attack [65,66]. For a carangiform robotic fish, however, its body and/or fins constantly undergo large deformation or rigid-body motion, and consequently, the angle of attack oscillates due to the body recoil. For these reasons, modeling variable drag coefficients is challenging, and existing work on robotic fish modeling has predominantly adopted constant drag coefficients [29,49,67]. In this paper, we propose a novel approach to adapting the drag coefficients. For ease of presentation, we focus on a robotic fish actuated by an oscillating tail, where the tail beat bias, frequency, and amplitude are the three kinematic parameters one can change. We first study the effect of each parameter on the average of the angle of attack, and find that the bias plays a much more significant role than the other two. We then propose determining the drag coefficients as simple polynomial functions of the tail beat bias. The effectiveness of the adaptation scheme is demonstrated through the comparison of simulation and experimental results, for both steady turning and transient dynamics in forward swimming.

The remainder of the paper is organized as follows. First, the dynamic model is described in Section 2. Experimental validation of the model is presented in Section 3. The drag coefficient adaptation scheme is discussed in Section 4. Finally, concluding remarks are provided in Section 5.

2. The dynamic model for robotic fish

The robot is considered to consist of two parts, a body that does not deform and a moving or deforming tail. The motion of the robot body is governed by rigid-body dynamics with the added-mass effect incorporated. Lighthill's large-amplitude elongated-body theory is utilized to evaluate the hydrodynamic forces generated by the actuating tail (as opposed to the whole robot). We assume that the depth of the tail does not change abruptly along the length direction, thus meeting the "elongated body" requirement [3]. Although the proposed modeling approach is applicable for a general actuating tail, for ease of presentation, we focus on the case where the tail is rigid and actuated at its base. As mentioned in Section 1, one contribution of this work lies in the *combination* of the two elements, rigid-body dynamics and Lighthill's theory, for the dynamic modeling of robotic fish. While both elements are well known, for completeness of the paper, brief review of each is provided in Sections 2.1 and 2.2.1, respectively.

2.1. Rigid-body dynamics

Fig. 1 shows the top view of the robotic fish, consisting of a rigid body and a tail. We follow [29] closely in describing the dynamics of the rigid body. $[X, Y, Z]$ denote the inertial coordinates while $[x, y, z]$ denote the body-fixed coordinates with unit vectors $[\hat{x}, \hat{y}, \hat{z}]$. We denote by $\hat{m}$ and $\hat{n}$ the unit vectors parallel and perpendicular to the tail, respectively. We assume that both the body and the tail are neutrally buoyant, and that, for the body, the center of gravity coincides with the center of geometry at point C. The velocity at C expressed in the body-fixed coordinates $\vec{V}_C = [V_{Cx}, V_{Cy}, V_{Cz}]^T$ comprises surge (V_{Cx}), sway (V_{Cy}) and heave (V_{Cz}) components. In addition, the angular velocity $\vec{\omega} = [\omega_x, \omega_y, \omega_z]^T$ comprises roll (ω_x), pitch (ω_y) and yaw (ω_z) expressed in the body-fixed coordinates. We use α to denote the tail deflection angle with respect to the negative x-axis, and β to denote the angle of attack, formed by the direction of $\vec{V}_C$ with respect to the x-axis. Finally, ψ denotes the heading angle, formed by the x-axis relative to the X-axis.

The linear momentum $\vec{P}$ and angular momentum $\vec{H}$ of the body in the body-fixed coordinates are expressed as

$$\vec{P} = \mathbf{M} \cdot \vec{V}_C + \mathbf{D}^T \cdot \vec{\omega}, \tag{1}$$

$$\vec{H} = \mathbf{D} \cdot \vec{V}_C + \mathbf{J} \cdot \vec{\omega}, \tag{2}$$

where $\mathbf{M}$ and $\mathbf{J}$ are the mass and inertia matrices, respectively, and $\mathbf{D}$ is the Coriolis and centripetal matrix. For a rigid body in an inviscid fluid, Kirchhoff's equations of motion in the body-fixed frame are [68,69]

$$\dot{\vec{P}} = \vec{P} \times \vec{\omega} + \vec{F}, \tag{3}$$

$$\dot{\vec{H}} = \vec{H} \times \vec{\omega} + \vec{P} \times \vec{V}_C + \vec{M}, \tag{4}$$

where $\vec{F} = [F_x, F_y, F_z]^T$, $\vec{M} = [M_x, M_y, M_z]^T$ denote the external forces and moments about the body center C, respectively, and "$\times$" denotes the vector product. The assumption of neural buoyancy implies that these forces and moments will only come from the hydrodynamic interactions between the robot and the fluid. We further assume that the body is symmetric with respect to the xz-plane and the tail moves in the xy-plane. Consequently, the heave velocity V_{Cz}, the roll rate ω_z, and the pitch rate ω_y are all equal to zero, in which case the system has three degrees of freedom, namely, surge

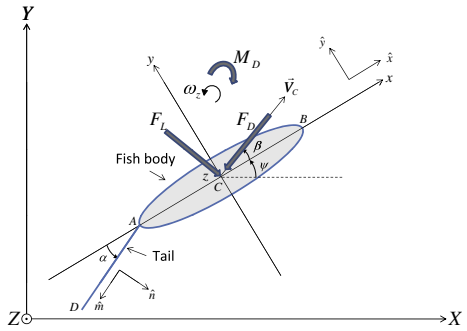

Fig. 1. Top view of the tail-actuated robotic fish undergoing planar motion.

(V_{Cx}), sway (V_{Cy}) and yaw (ω_z). We further assume that the inertial coupling between the surge, sway and yaw motions is negligible [29], implying $\mathbf{D} = 0$. Under these assumptions, following [68], (3) and (4) can be simplified as

$$(m_b - X_{\dot{V}_{Cx}})\dot{V}_{Cx} = (m_b - Y_{\dot{V}_{Cy}})V_{Cy}\omega_z + F_x, \tag{5}$$

$$(m_b - Y_{\dot{V}_{Cy}})\dot{V}_{Cy} = -(m_b - X_{\dot{V}_{Cx}})V_{Cx}\omega_z + F_y, \tag{6}$$

$$(J_{bz} - N_{\dot{\omega}_z})\dot{\omega}_z = (Y_{\dot{V}_{Cy}} - X_{\dot{V}_{Cx}})V_{Cx}V_{Cy} + M_z, \tag{7}$$

where m_b is the mass of the body, and J_{bz} is the inertia of the body about the z-axis. $X_{\dot{V}_{Cx}}$, $Y_{\dot{V}_{Cy}}$ and $N_{\dot{\omega}_z}$ are the hydrodynamic derivatives that represent the effect of added mass/inertia on the body.

2.2. Evaluation of the hydrodynamic forces

To complete the model (5)–(7), we need to evaluate the hydrodynamic force (F_x, F_y) and moment M_z, which are due to both the tail actuation and the interaction of the body itself with the fluid. We first review Lighthill's large-amplitude elongated-body theory, and use it to evaluate the forces exerted on the tail (and transmitted to the rigid body) due to tail-fluid interactions. The drag and lift forces on the robotic fish body will then be described.

2.2.1. Lighthill's large-amplitude elongated-body theory

Consider an elongated "body" moving in the XY-plane in water; here (and throughout Section 2.2.1) the term "body" could mean a live fish, a robotic fish, or in the context of our work, a flapping tail. As illustrated in Fig. 2, a frame of reference is chosen such that the water far from the body is at rest. The spinal column (analogy from a live fish) of the elongated body is assumed to be inextensible and is parameterized by τ, with $\tau = 0$ denoting the anterior end of the body and $\tau = L$ denoting the posterior end. The coordinates $(X(\tau, t), Y(\tau, t))$, $0 \leqslant \tau \leqslant L$, denote the trajectory of each point τ on the spinal column at time t, which could be due to the body undulation/oscillation or the resulting translational/rotational motion of the body.

Following [3], given $(X(\tau, t), Y(\tau, t))$, the hydrodynamic reactive force density at each point $\tau < L$, due to the added-mass effect, is

$$\vec{f}(\tau) = \begin{pmatrix} f_X(\tau) \\ f_Y(\tau) \end{pmatrix} = -m\frac{\mathrm{d}}{\mathrm{d}t}(v_\perp \hat{n}), \tag{8}$$

and at $\tau = L$, there is a concentrated force

$$\vec{F}_L = \begin{pmatrix} F_{LX} \\ F_{LY} \end{pmatrix} = \left[-\frac{1}{2}m v_\perp^2 \hat{m} + m v_\perp v_\parallel \hat{n}\right]_{\tau=L}. \tag{9}$$

The two terms in (9) account for the pressure force acting on Π and the force due to convection of momentum out of $\mathscr{V}$ across Π, respectively, where Π is the plane at $\tau = L$ that is perpendicular to $\hat{m}$, and $\mathscr{V}$ is the half-space bounded by Π that includes the fish but excludes the wake [3]. In (8) and (9), m denotes the virtual mass per unit length and can be approximated by $\frac{1}{4}\pi\rho d^2$, where ρ is the density of water and d is the depth of fish cross-section (in $-Z$ direction) at τ (and thus can vary with τ). As illustrated in Fig. 2, $\hat{m} = (\partial X/\partial\tau, \partial Y/\partial\tau)^T$ and $\hat{n} = (-\partial Y/\partial\tau, \partial X/\partial\tau)^T$ represent the unit vectors tangential and perpendicular to the spinal column, respectively, and $v_\parallel$ and $v_\perp$ represent the components of the velocity $\vec{v} = (\partial X/\partial t, \partial Y/\partial t)^T$ at τ in $\hat{m}$ and $\hat{n}$ directions, respectively:

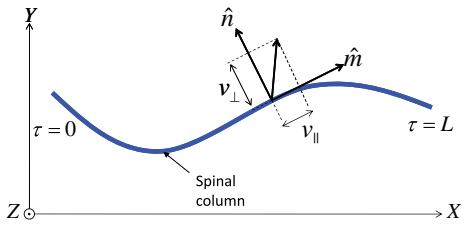

Fig. 2. Illustration of the coordinate system for the spinal column of the elongated body (top view).

$$v_\parallel = \langle \vec{v}, \hat{m} \rangle = \frac{\partial X}{\partial t}\frac{\partial X}{\partial \tau} + \frac{\partial Y}{\partial t}\frac{\partial Y}{\partial \tau}, \tag{10}$$

$$v_\perp = \langle \vec{v}, \hat{n} \rangle = -\frac{\partial X}{\partial t}\frac{\partial Y}{\partial \tau} + \frac{\partial Y}{\partial t}\frac{\partial X}{\partial \tau}, \tag{11}$$

where $\langle \cdot, \cdot \rangle$ denotes the inner product of vectors. Note that the actual mass of the considered elongated-body is negligible (relative to the virtual mass) when the width of the body cross-section is much thinner than the depth [3]. The latter typically holds true for the tail of a robotic fish.

2.2.2. Hydrodynamic force due to an oscillating tail

Following Lighthill's large-amplitude elongated-body theory, we need to know the motion of every point along the tail over time, to evaluated the tail actuation-induced hydrodynamic force.

Refer to Fig. 1. The velocity $\vec{V}_A$ at the body-tail joint A can be expressed as

$$\vec{V}_A = \vec{V}_C - \omega_z c\hat{y}, \tag{12}$$

where c is the distance from the body center to the joint. The velocity at each point τalong the tail is

$$\vec{V}_\tau = \vec{V}_C - \omega_z c\hat{y} + (\dot{\alpha} + \omega_z)\tau\hat{n}, \tag{13}$$

where $\dot{\alpha}$ denotes the angular velocity of the tail with respect to the body. Note here that $\tau = 0$ would represent the point A. In (13), $\vec{V}_\tau$ is calculated incorporating the robot body motion ($\vec{V}_C$ and ω_z), which is often ignored in the literature [28,29,64]. In Section 3.4, we will discuss the role of incorporating the body motion in the appropriate evaluation of hydrodynamic forces.

Let $\vec{V}_{\tau_\perp}$ be the projection of $\vec{V}_\tau$ along the $\hat{n}$ direction, i.e., $\vec{V}_{\tau_\perp} = \langle \vec{V}_\tau, \hat{n} \rangle \hat{n}$. Using (8), we evaluate the hydrodynamic force density at τ as

$$\vec{f}(\tau) = -m\frac{\mathrm{d}\vec{V}_{\tau_\perp}}{\mathrm{d}t}. \tag{14}$$

Then the hydrodynamic force on the tail due to the added-mass effect is

$$\vec{F}_a = \int_0^L \vec{f}(\tau)\mathrm{d}\tau = F_{am}\hat{m} + F_{an}\hat{n}, \tag{15}$$

where L is the length of the tail, and $F_{a\,m}$ and $F_{a\,n}$ are the components of F_a along $\hat{m}$ and $\hat{n}$, respectively.

From (9), the concentrated force acting at the tail tip is evaluated as $\vec{F}_c = F_{c1}\hat{m} + \vec{F}_{c2}\hat{n}$, where

$$F_{c1} = -\frac{1}{2}mV_{L_\perp}^2,$$

$$F_{c2} = mV_{L_\perp}V_{L_\parallel}.$$

The total hydrodynamic force acting on the tail is then

$$\vec{F}_h = F_{hx}\cdot\hat{x} + F_{hy}\cdot\hat{y},$$

where

$$F_{hx} = -(F_{am} + F_{c1})\cos\alpha + (F_{an} + F_{c2})\sin\alpha, \tag{16}$$

$$F_{hy} = -(F_{am} + F_{c1})\sin\alpha - (F_{an} + F_{c2})\cos\alpha. \tag{17}$$

The hydrodynamic force-induced moment relative to the center C of the robot body is

$$\vec{M}_h = \int_0^L \vec{r}_{C\tau} \times \vec{f}(\tau)\,\mathrm{d}\tau + \vec{r}_{CL} \times \vec{F}_c, \tag{18}$$

where $\vec{r}_{C\tau}$ denotes the vector from the body center C to the point τ on the tail, i.e., $\vec{r}_{C\tau} = -(c + \tau\cos\alpha)\hat{x} - (\tau\sin\alpha)\hat{y}$. It is clear that all

vectors in (18) lie in the xy-plane, and thus the only non-zero component of $\vec{M}_h$ is along the z-direction, which we denote as M_{hz}.

2.2.3. Drag and lift on the body

As shown in Fig. 1, besides the hydrodynamic force and moment transmitted from the tail, the robot body also experiences drag force F_D, lift force F_L, and drag moment M_D [24,29,49]:

$$F_D = \frac{1}{2}\rho|V_C|^2 S C_D, \tag{19}$$

$$F_L = \frac{1}{2}\rho|V_C|^2 S C_{L\beta}\beta, \tag{20}$$

$$M_D = -K_D\omega_z^2 \mathrm{sgn}(\omega_z). \tag{21}$$

where S is a suitably defined reference surface area for the robot body. C_D and K_D are the drag force coefficient and drag moment coefficient, respectively. $C_{L\beta}$ is the lift coefficient per angle of attack β. The drag coefficients, as we will discuss later, are generally dependent on the angle of attack β of the robot body.

Finally, by adding the hydrodynamic forces and moments from the tail and directly on the body, we obtain F_x, F_y, and M_z in (5)–(7) as

$$F_x = F_{hx} - F_D\cos\beta + F_L\sin\beta, \tag{22}$$

$$F_y = F_{hy} - F_D\sin\beta - F_L\cos\beta, \tag{23}$$

$$M_z = M_{hz} + M_D. \tag{24}$$

3. Experimental model validation

3.1. Experimental setup

To validate the proposed dynamic model in Section 2, experiments have been conducted with a free-swimming robotic fish prototype as shown in Fig. 3. The robot has a simple mechanism for actuation, and it satisfies most of the assumptions used in the modeling work, which facilitates model validation. Through a chain transmission mechanism, a servomotor (HS-5085MG from Hitec) was used to control the angular position of the tail shaft and thus the tail deflection angle α. The tail was a rectangular carbon-fiber foil, which was 8 cm long, 2.5 cm wide (deep), and 1.1 mm thick. With an onboard microcontroller, the servomotor was programmed to rotate the tail according to

$$\alpha(t) = \alpha_0 + \alpha_A\sin(\omega_\alpha t + \phi_\alpha) \tag{25}$$

with α_0, α_A and ω_α denoting the bias, amplitude, and frequency of the tail beat, respectively; and ϕ_α denoting the phase that indicates the initial condition. When the bias $\alpha_0 = 0$, the robot performs forward swimming. When $\alpha_0 \neq 0$, the trajectory of the robot converges to a circular orbit. For model validation, we measured the turning radius (radius of the circular orbit) and turning period (time for completing a turn) during steady turning, under different combinations of α_0, α_A, and ω_α. The experiments were conducted in an indoor kiddie pool (as shown in Fig. 7 of [62]), and the turning radius and period were measured with a timer and yardstick, respectively. Specifically, for each experiment, we would first wait until the robot entered steady turning, and then place a yardstick (suspended slightly higher than the top of the robot) along the line connecting the visually determined leftmost and rightmost points of the trajectory. Afterwards (while the robot continued turning) we would mark down the points A and B where the robot entered and left, respectively, the half-space defined by the yardstick. These two points were typically close to the visually determined left/rightmost points mentioned earlier. The distance between A and B and the difference between the times when the robot hit these two points (captured by a timer) were used to determine the turning radius and period, respectively. With any prescribed open-loop control pattern, the observed circular orbit shifted slightly over time, which could be due to the flow disturbance created by the swimming robot in the relatively small pool (diameter 1.75 m). To mitigate the impact of such shift on the measurement error, for each pattern, experiments were repeated for 6 times (restarting the robot from rest every time), from which the mean and standard deviation of the turning radius/period were evaluated. We note that, while the turning experiments conducted in this work did offer valuable insight on how tail-beat parameters could impact turning behavior, their primary use is in providing data for model validation under a wide range of open-loop inputs. This is different from [70], where the authors focused on turning control strategies for multi-link robotic fish.

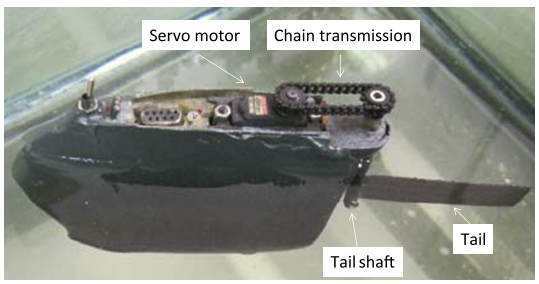

Fig. 3. A free-swimming robotic fish prototype used for model validation.

3.2. Parameter identification

The parameters in simulation are measured directly or calculated based on measurement as shown in Table 1. The body inertia about the z-axis is evaluated as $J_{bz} = \frac{1}{12}m_b(2c)^2$. The added masses and inertia are calculated by approximating the robot body as a prolate spheroid [29,69].

The drag and lift coefficients C_D, $C_{L\beta}$, and K_D can be potentially obtained by performing tests in a water tunnel or from the CFD simulation, while in this work, we choose a more efficient way to empirically identify these coefficients. In particular, we have tuned these parameters to match the turning radius, turning period, and the average of $|\beta|$ obtained in simulation with the experimental measurement under a particular tail beat pattern, with bias $\alpha_0 = 20°$, amplitude $\alpha_A = 15°$, and frequency $\omega_A = 1.8\pi$ rad/s (0.9 Hz). The resulting coefficients are $C_D = 0.2231$, $C_{L\beta} = 4.50$, and $K_D = 11.29 \times 10^{-4}$ kg m^2. These parameters are then used in independent model validation for all other tail beat patterns.

3.3. Results on model validation

Figs. 4–6 show the comparison between the model prediction and experimental measurement of the turning radius and turning

Table 1
Parameter values for simulations.

Component	Parameter	Value
Body	Mass (m_b)	0.311 kg
	Distance from body center to the shaft (c)	0.07 m
	Nominal body surface area (S)	0.0108 m^2
	Inertia (J_{bz})	5.0797×10^{-4} kg m^2
	$-X_{\dot{V}_{Cx}}$	0.0621 kg
	$-Y_{\dot{V}_{Cy}}$	0.2299 kg
	$-N_{\dot{\omega}_z}$	1.0413×10^{-4} kg m^2
Tail	Tail length (L)	0.08 m
	Tail depth (d)	$d = 0.025$ m
	Water density (ρ)	1×10^3 kg/m^3

period, when we vary the tail beat bias α_0, amplitude α_A, and frequency ω_α, respectively, while holding the other two parameters constant.

Experimental results in Fig. 4 show that both the turning radius and the turning period drop monotonically with an increasing tail beat bias; in other words, the robot makes tighter and quicker turns as the bias is increased. For these experiments, the tail beat amplitude and frequency are held fixed at 15° and 0.9 Hz, respectively. From Fig. 4, these trends are well captured by the model prediction, which closely matches the experimental measurement.

Fig. 5 shows how the turning radius and period depend on the tail beat amplitude, where the bias and frequency are set to be 20° and 0.9 Hz, respectively. The model predicts that the turning radius is nearly constant (about 27.5 cm) over the tested range for the tail beat amplitude. The mean of the measured radii for each given amplitude stays within the band [26] cm, which is close to the predicted value. The turning period is predicted by the model to decrease (i.e., faster turning) as the tail beat amplitude increases, which is supported by the experimental data both qualitatively and quantitatively.

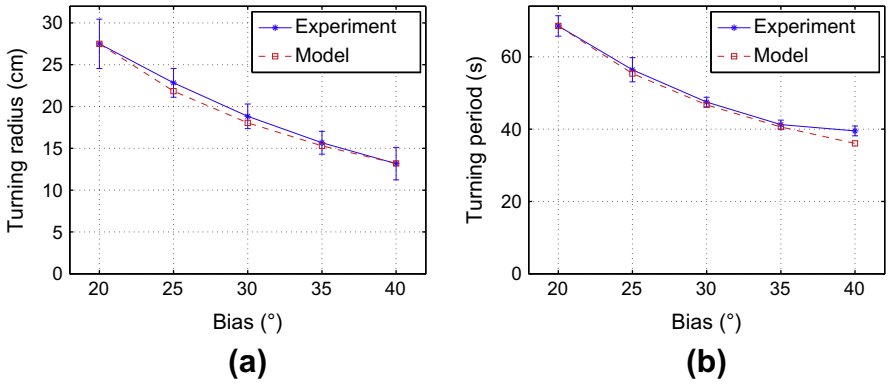

Fig. 4. Comparison between model prediction and experimental measurement of (a) turning radius and (b) turning period as a function of the tail beat bias α_0. The amplitude and frequency of the tail beat are fixed at 15° and 0.9 Hz, respectively.

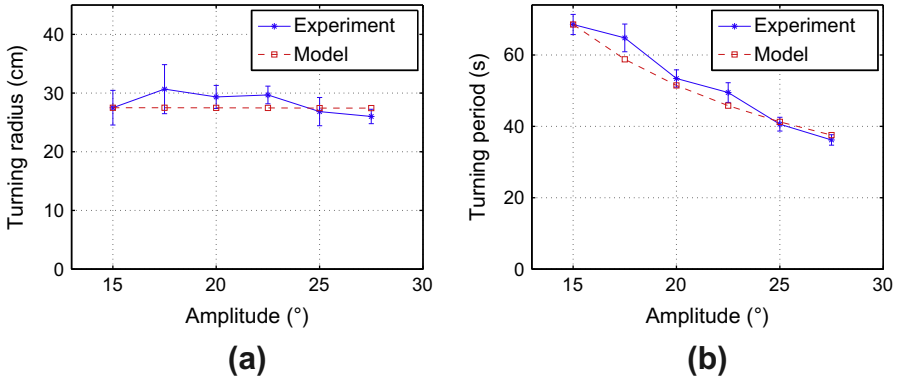

Fig. 5. Comparison between model prediction and experimental measurement of (a) turning radius and (b) turning period as a function of the tail beat amplitude. The bias and frequency of the tail beat are fixed at 20° and 0.9 Hz, respectively.

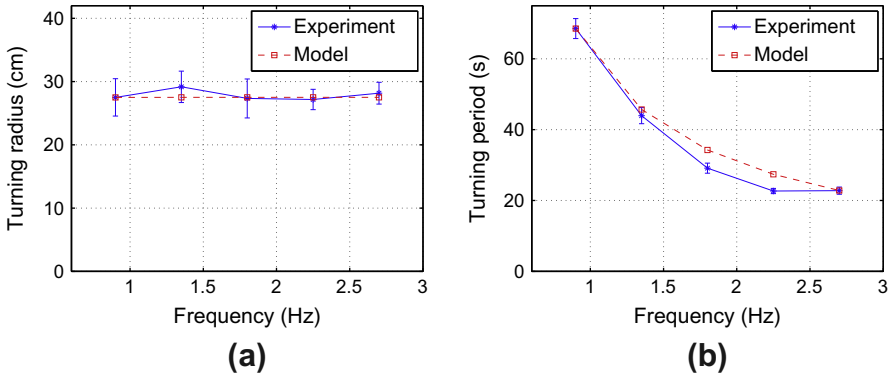

Fig. 6. Comparison between model prediction and experimental measurement of (a) turning radius and (b) turning period as a function of the tail beat frequency. The bias and amplitude of the tail beat are fixed at 20° and 15°, respectively.

The impact of the tail beat frequency on the turning behavior is shown in Fig. 6, where the chosen tail beat bias and amplitude are 20° and 15°, respectively. The model predicts that the turning radius has negligible dependence on the tail frequency, while the turning period drops with the frequency. As seen in Fig. 6, both trends are well supported by the experimental data.

3.4. Hydrodynamic forces with/without incorporating robotic fish body motion

It is often tempting to consider the body as anchored when evaluating fin-produced hydrodynamic forces [64,29,28], since this would greatly simplify the model. It is of interest to assess the validity of such simplifications for a free-swimming robot where the robot body undergoes movement. We will use the proposed model in Section 2, which has proven effective as shown in the previous subsection, to evaluate the necessity of incorporating the body motion, by comparing the simulation results when such motion is and is not considered.

For this study, we take the tail beat bias α_0 to be 0, and thus the robot will perform forward swimming at the steady state. We will evaluate the impact of incorporating (or neglecting) body motion on the computed average thrust (over a tail-beat cycle) and the robot swimming speed. The thrust force is evaluated via

$$F_{thrust} = F_{hx}\cos(\psi - \psi_0) - F_{hy}\sin(\psi - \psi_0), \tag{26}$$

where we recall from Fig. 1 that ψ denotes the heading of the robotic fish with respect to the X-axis in the inertial frame. In (26), ψ_0 denotes the average of ψ over a tail-beat cycle at the steady state, while F_{hx} and F_{hy} are evaluated using (16) and (17). Ignoring the body motion in hydrodynamic force evaluation implies that the velocity $\vec{V}_\tau$ at point τ on the tail is changed from (13) to

$$\vec{V}_\tau = \dot{\alpha}\tau\hat{n}. \tag{27}$$

Fig. 7 compares the calculated average thrusts under different tail-beat amplitudes and frequencies, when the body motion is and is not incorporated in evaluating $\vec{V}_\tau$, respectively. It shows clearly that ignoring the body motion would result in significant over-estimate of the thrust. For example, when the tail beats at 0.9 Hz with an amplitude of 15°, the average thrust is 1.188 mN when the body motion is ignored, which is 57% larger than the value of 0.755 mN when the body motion is considered. Fig. 8 further compares the computed average swimming speeds under the two modeling schemes, from which we can see that ignoring the body motion results in an over-estimate of steady-state speed by about 25%. These results illustrate the profound impact of the body motion on the tail-generated hydrodynamic force.

4. Efficient adaptation of drag coefficients

4.1. Bias-based adaptation of drag coefficients

The drag force and moment coefficients C_D and K_D in (19) and (21) have been assumed to be constants. Most (if not all) modeling work on robotic fish has assumed constant drag coefficients [29,49,50,67]. However, it is known in fluid mechanics that the angle of attack influences the drag on a body that is moving through a

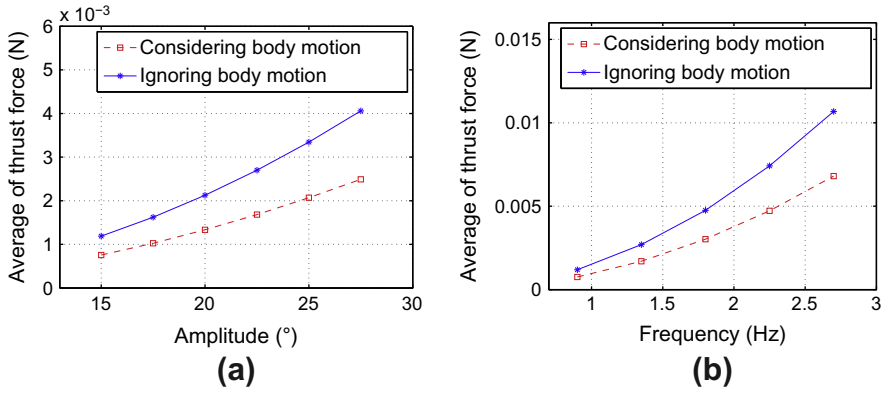

Fig. 7. Simulated average thrust force with/without incorporating the body motion: (a) thrust force versus tail-beat amplitude (frequency fixed at 0.9 Hz); (b) thrust force versus tail-beat frequency (amplitude fixed at 15°).

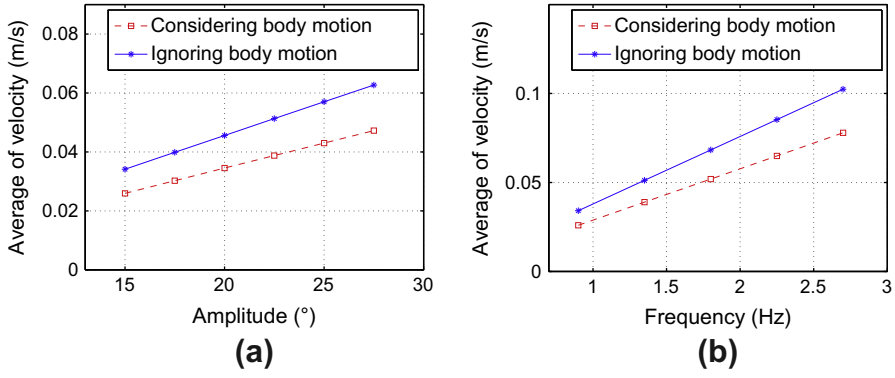

Fig. 8. Simulated average velocity with/without incorporating the body motion: (a) velocity versus tail-beat amplitude (frequency fixed at 0.9 Hz); (b) velocity versus tail-beat frequency (amplitude fixed at 15°).

fluid [24,50,65,66]. For robotic fish, one challenge is that the angle of attack oscillates constantly because of the recoil motion of the body in response to tail movements. Furthermore, evaluation of the angle of attack involves a highly non-linear function of the velocity components, $\beta = \arctan(V_{Cy}/V_{Cx})$. In this section, we present an approach to the efficient adaptation of drag coefficients for robotic fish, to maintain or even improve model fidelity without the need to explicitly evaluate the angle of attack. The word "efficient" here refers to computational efficiency (or low modeling complexity), as we will show in the later part of this section that such a varying drag effect can be well captured with a simple function of the tail-beat bias.

At the core of our approach is the exploitation of the close correlation between the angle of attack and the tail beat bias. Recall the form of the tail beat angle α in (25). While the bias α_0, amplitude α_A, and frequency ω_α all could be varied over time (for example, when one controls the robot to follow some arbitrary path), such variations typically take place at a much slower time scale than the tail beat motion – a tail beat pattern will be repeated for at least several cycles before it is updated. Figs. 4–6 suggest that the turning radius strongly depends on the bias α_0, but is nearly independent of the amplitude α_A and frequency ω_α. The turning radius is intimately related to the angle of attack. To explicitly reveal the relationships between the angle of attack and the tail-beat pattern parameters, we have used the model identified in Section 3 to numerically evaluate the average β_0 of the absolute value $|\beta|$ of the angle of attack over each beat cycle, i.e.,

$$\beta_0 = \frac{\omega_\alpha}{2\pi}\int_{t_0}^{t_0+2\pi/\omega_\alpha} |\beta(t)|\mathrm{d}t. \tag{28}$$

From Fig. 9, β_0 shows nearly linear dependence on the tail-beat bias angle, with little dependence on the amplitude or the frequency.

Based on the observations from Fig. 9 and on the relationships between the drag coefficients and the angle of attack [65], we propose adapting these coefficients using the tail-beat bias α_0 (note that the underlying assumption here is that, the impact of the angle of attack, β, on drag can be well captured through the cycle-averaged absolute value of β, β_0):

$$C_D = C'_{D0} + C'_{D1}\alpha_0^2, \tag{29}$$
$$K_D = K'_{D0} + K'_{D1}\alpha_0, \tag{30}$$

where C'_{D0}, C'_{D1}, K'_{D0} and K'_{D1} are constants that are empirically identified as follows. First, as described in Section 3.2, we seek values of C_D, K_D, and $C_{L\beta}$ such that the simulated turning radius and period best match the experimental results when the tail beats at 0.9 Hz with amplitude of 15° and bias of 20°. We then maintain the value of $C_{L\beta}$, and find the best parameter estimates for C_D and K_D when the bias is 30° and 40°, respectively. We have deliberately left out the cases of 25° and 35° biases at this stage, so that those data can be used in independent model validation. Table 2 lists the identified C_D and K_D identified for the three biases. We then use the values in Table 2 to identify C'_{D0}, C'_{D1}, K'_{D0} and K'_{D0} in (29) and (30) through the least-square-error fitting. The resulting parameters are $C'_{D0} = 0.1936$, $C'_{D1} = 0.1412/\mathrm{rad}^2$, $K'_{D0} = 9.655 \times 10^{-4}$ kg m^2 and $K'_{D1} = 4.383 \times 10^{-4}$ kg m^2/rad, respectively.

Fig. 10 shows the comparison between the measured turning radii and periods and the values predicted by the model with drag coefficient adaptation. We can see that, with the bias-based adaptation of drag coefficients, the match between the model prediction and the experimental data is further improved over that in Fig. 4.

To further validate the approach for drag coefficient adaptation, we have conducted additional experiments involving transients in forward swimming. A yellow LED powered by a button cell was taped to the top of the robot as a marker. The weight of the LED/cell add-on was 3 g, so its impact on the total mass (over 300 g) and inertia of the robot was negligible. Starting from at rest, the robot was programmed to swim forward (with the tail beat bias $\alpha_0 = 0°$) with the amplitude and frequency of the tail-beat equal to 15° and 0.9 Hz, respectively. We video-recorded the motion of the LED (and thus of the robot) with the ambient light turned off, and extracted the robot's time-trajectory by applying background subtraction to the images. The dynamic model has been simulated with the adapted and non-adapted drag coefficients, respectively. For the model with non-adapted drag coefficients, $C_D = 0.2231$, $K_D = 11.29 \times 10^{-4}$ kg m^2, which are identical to the coefficients obtained from the turning experiments as presented in Section 3.2. For the model with adapted drag coefficients, $C_D = 0.1936$, $K_D = 9.655 \times 10^{-4}$ kg m^2, which are evaluated based on (29) and (30), with $\alpha_0 = 0$. Fig. 11(a) and (b) compare the model predictions of the X/Y-coordinate time-trajectories of the robot with the experimental measurement, and Fig. 11(c) provides the comparison on the robot path in the XY-plane. It can be seen that the model with adapted drag coefficients outperforms the one with non-adapted coefficients, and is able to capture well both the transient and steady-state behaviors of the robot.

Table 2
Identified drag force and moment coefficients for different tail beating biases.

Bias α_0 (°)	C_D	K_D (kg m^2)
20	0.2231	1.129×10^{-3}
30	0.2112	1.174×10^{-3}
40	0.2712	1.282×10^{-3}

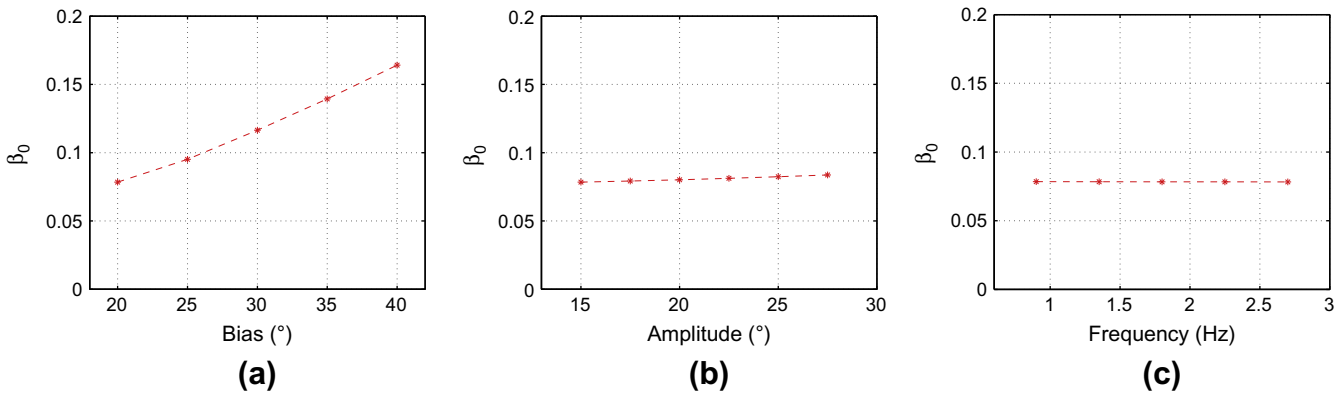

Fig. 9. Simulation results on the dependence of the angle of attack on tail beat parameters, where β_0 is the cycle-averaged absolute value of the angle attack: (a) β_0 versus the tail beat bias α_0; (b) β_0 versus the tail beat amplitude α_A; (c) β_0 versus the tail beat frequency ω_α. In (a), the amplitude and frequency are fixed at 15° and 0.9 Hz; in (b), the bias and the frequency are fixed at 20° and 0.9 Hz; in (c), the bias and the amplitude are fixed at 20° and 15°.

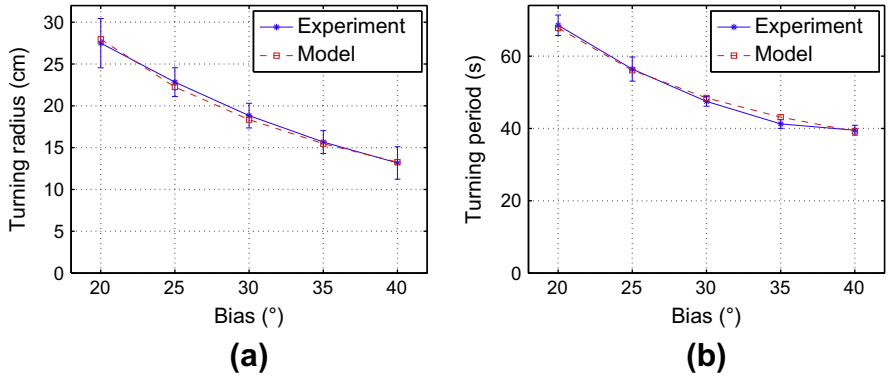

Fig. 10. Comparison between experimental measurement of (a) turning radius and (b) turning period with those predicted by the model, where the drag coefficients are adapted and the lift force is evaluated using (20). The amplitude and frequency of the tail beat are fixed at 15° and 0.9 Hz, respectively.

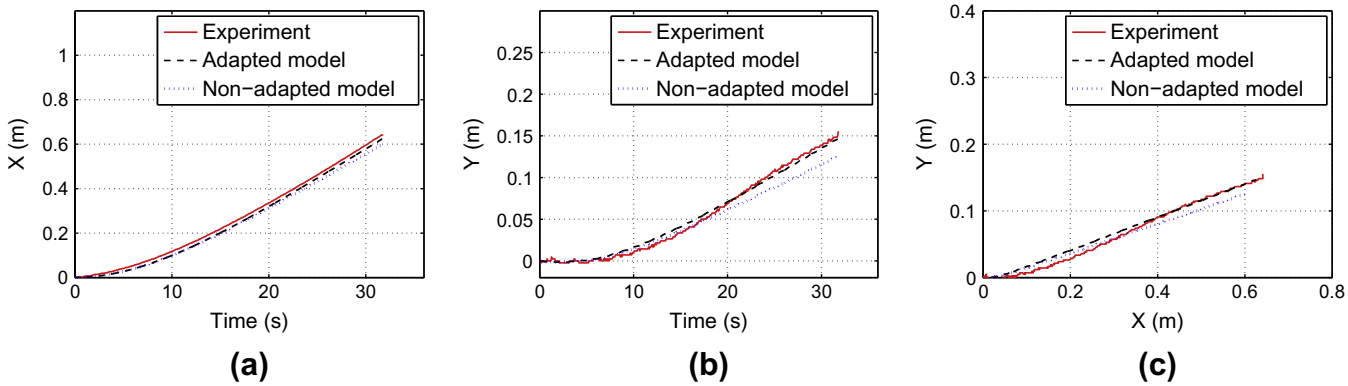

Fig. 11. Comparison between model predictions and experimental measurement for forward swimming (including transients): (a) time trajectory of X-coordinate of the robot; (b) time trajectory of the Y-coordinate of the robot; (c) path of the robot in the XY-plane. For both the experiment and simulations, the amplitude and frequency of the tail beat are fixed at 15° and 0.9 Hz, respectively.

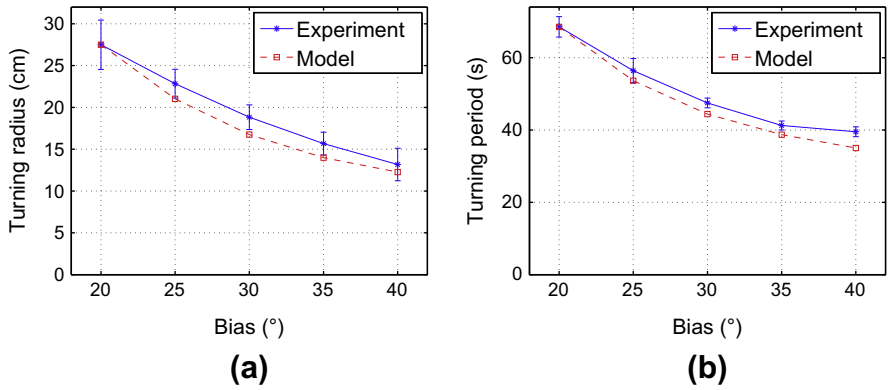

Fig. 12. Comparison between experimental measurement of (a) turning radius and (b) turning period with those predicted by the model, where the drag coefficients are not adapted and the lift force is evaluated using (31). The amplitude and frequency of the tail beat are fixed at 15° and 0.9 Hz, respectively.

4.2. Elimination of the angle of attack from the lift force term

Note that, while the drag coefficients in (29) and (30) do not involve the angle of attack β, the evaluation of the lift force for the robot body in (20) still requires knowing β. In order to eliminate β from the overall model and thus reduce the model complexity, in this subsection we explore replacing β in (20) with the tail-beat bias α_0:

$$F_L = \frac{1}{2}\rho|V_C|^2 S C'_{L\beta}\alpha_0, \tag{31}$$

where, $C'_{L\beta}$ is the new lift coefficient associated with the tail bias. To identify $C'_{L\beta}$, we tune $C'_{L\beta}$, C_D, and K_D so that the simulated turning radius, turning period, and average of $|\beta|$ match those obtained in experiments when the tail beats with bias $\alpha_0 = 20°$, amplitude $\alpha_A = 15°$, and frequency $\omega_A = 1.8\pi$ rad/s. The estimates are $C'_{L\beta} = 0.935$, $C_D = 0.2131$, and $K_D = 1.144 \times 10^{-3}$ kg m^2. With $C'_{L\beta}$ fixed, we can then follow the similar steps as in Section 4.1 to determine the drag coefficient adaptation laws (29) and (30). Note that the four parameters in (29) and (30) are identified twice since we want to compare the two cases when the evaluation of the lift force

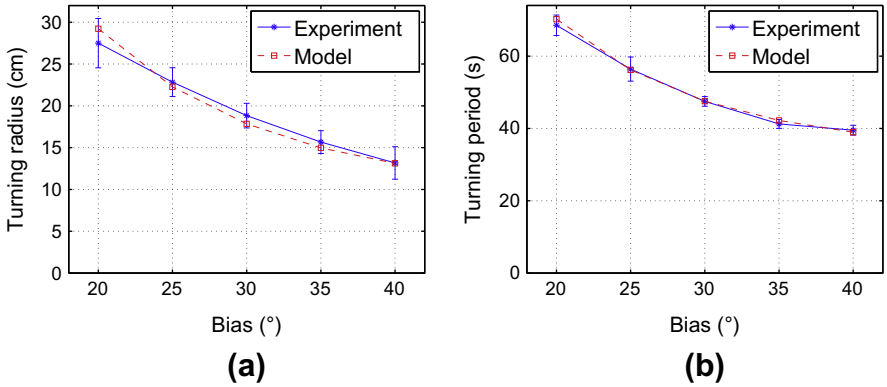

Fig. 13. Comparison between experimental measurement of (a) turning radius and (b) turning period with those predicted by the model, where the drag coefficients are adapted and the lift force is evaluated using (31). The amplitude and frequency of the tail beat are fixed at 15° and 0.9 Hz, respectively.

involves the angle of attack β or its surrogate α_0. In practice, one only needs to identify these parameters once given the choice of (20) or (31) for the lift force evaluation.

Figs. 12 and 13 show the model prediction performance when drag coefficients are fixed and adapted, respectively, where the lift force is evaluated using (31) instead of using (20) as for Figs. 4, 5, 6 and 10. From Fig. 12, the model with the modified lift term (31) is still able to capture the trends of how the turning radius and period vary with the tail bias, although the match has degraded from that seen in Fig. 4. From Fig. 13, one can see that, with the drag adaption, significantly better match between the model prediction and experimental data is achieved.

5. Conclusion

In this paper, we have presented a complete dynamic model for robotic fish actuated by a caudal fin, where Lighthill's elongated-body theory is used to evaluate the tail-generated hydrodynamic force. For experimental validation purpose, we have considered a rigid tail with biased sinusoid oscillation and treated the turning radius and turning period as outputs in the comparison between model prediction and experimental results. Additional model validation has also been conducted with experimental data of forward swimming including the transients. We have found that, incorporating the body motion in the evaluation of hydrodynamic forces plays a significant role in capturing the dynamics. We have also shown that, the drag force and moment coefficients are strongly dependent on the tail-beat bias, and subsequently we have proposed a novel scheme to adapt these coefficients and lift force based on the tail movement pattern. The effectiveness of this approach has been further demonstrated in experiments.

There are several directions in which the current work can be extended. First, this paper has been primarily concerned with a rigid tail. It is of interest to extend the results to the case of a base-actuated flexible tail, where the vibrational dynamics of the tail is coupled to the hydrodynamics and adds complexity to the evaluation of tail-generated force and moment. It has been recognized that the flexibility of body and fin structures has a pronounced impact on the swimming performance of biological and robotic fish [71–73], and the insight from these studies will be useful in the modeling and optimization of a flexible tail for robotic fish. Second, with the caudal fin as the only actuator, the presented model was limited to the planar motion. Three-dimensional (3D) maneuvers (e.g., diving and ascent) are often of practical interest and can be realized by incorporating actuation mechanisms to adjust buoyancy or center of gravity. Other actuating fins, in particular, pectoral fins, can also enhance maneuverability of the robot (at the cost of complexity). It is worthwhile to examine how the presented model in this paper can be expanded to capture the 3D dynamics and account for these additional actuation effects.

Acknowledgment

The authors thank John Thon for his contribution to the building of the robotic fish prototype used in this work, and Freddie Alequin-Ramos for collecting data on the turning experiments.

References

[1] Lauder GV, Drucker EG. Morphology and experimental hydrodynamics of fish fin control surfaces. IEEE J Ocean Eng 2004;29(3):556–71.
[2] Fish FE, Lauder GV. Passive and active flow control by swimming fishes and mammals. Annu Rev Fluid Mech 2006;38:193–224.
[3] Lighthill MJ. Large-amplitude elongated-body theory of fish locomotion. Proc Roy Soc Lond B 1971;179:125–38.
[4] Wu TY. Hydromechanics of swimming propulsion. Part 1. Swimming of a two-dimensional flexible plate at variable forward speeds in an inviscid fluid. J Fluid Mech 1971;46:337–55.
[5] Kanso E. Swimming due to transverse shape deformations. J Fluid Mech 2009;631:127–48.
[6] Ahlborn B, Chapman S, Stafford R, Blake RW, Harper DG. Experimental simulation of the thrust phase of fast-start swimming of fish. J Exp Biol 2007;200:2301–12.
[7] Spierts ILY, Van Leeuwen JL. Kinematics and muscle dynamics of C- and S-starts of carp (cyprinus carpio l.). J Exp Biol 1999;202:393–406.
[8] Muller UK, Stamhuis EJ, Videler JJ. Riding the waves: the role of the body wave in undulatory fish swimming. Integr Compar Biol 2002;42:981–7.
[9] Triantafyllou MS, Yue DKP, Triantafyllou GS. Hydrodynamics of fishlike swimming. Annu Rev Fluid Mech 2000;32:33–53.
[10] Triantafyllou MS, Techet AH, Hover FS. Review of experimental work in biomimetic foils. IEEE J Ocean Eng 2004;29(3):585–94.
[11] Liu H, Wassersug RJ, Kawachi K. A computational fluid dynamics study of tadpole swimming. J Exp Biol 1996;199:1245–60.
[12] Mittal R. Computational modeling in biohydrodynamics: trends, challenges, and recent advances. IEEE J Ocean Eng 2004;29(3):595–604.
[13] Triantafyllou MS, Triantafyllou GS. An efficient swimming machine, vol. 272. Scientific American; 1995. p. 64.
[14] Byun D, Choi J, Cha K, Park J, Park S. Swimming microrobot actuated by two pairs of helmholtz coils system. Mechatronics 2011;21(1):357–64.
[15] Kato N. Control performance in the horizontal plane of a fish robot with mechanical pectoral fins. IEEE J Ocean Eng 2000;25(1):121–9.
[16] Anderson JM, Chhabra NK. Maneuvering and stability performance of a robotic tuna. Integ Comp Biol 2002;42:118–26.
[17] Bandyopadhyay PR. Maneuvering hydrodynamics of fish and small underwater vehicles. Integ Comp Biol 2002;42:102–17.
[18] Yu J, Tan M, Wang S, Chen E. Development of a biomimetic robotic fish and its control algorithm. IEEE Trans Syst Man Cybernet: Part B 2004;34(4):1798–810.
[19] Long JH, Lammert AC, Pell CA, Kemp M, Strother JA, Crenshaw HC, et al. A navigational primitive: biorobotic implementation of cycloptic helical klinotaxis in planar motion. IEEE J Ocean Eng 2004;29(3):795–806.
[20] Alvarado PV, Youcef-Toumi K. Design of machines with compliant bodies for biomimetic locomotion in liquid environments. J Dynam Syst Measur Contr 2006;128:3–13.
[21] Liu J, Hu H. Biologically inspired behavior design for autonomous robotic fish. Int J Automat Comput 2006;4:336–47.

[22] Epstein M, Colgate JE, MacIver MA. Generating thrust with a biologically-inspired robotic ribbon fin. In: Proceedings of the 2006 IEEE/RSJ international conference on intelligent robots and systems, Beijing, China; 2006. p. 2412–7.
[23] Krieg M, Mohseni K. Dynamic modeling and control of biologically inspired vortex ring thrusters for underwater robot locomotion. IEEE Trans Robot 2010:542–54.
[24] Morgansen KA, Triplett BI, Klein DJ. Geometric methods for modeling and control of free-swimming fin-actuated underwater vehicles. IEEE Trans Robot 2007;23(6):1184–99.
[25] Lauder GV, Anderson EJ, Tangorra J, Madden PGA. Fish biorobotics: kinematics and hydrodynamics of self-propulsion. J Exp Biol 2007;210:2767–80.
[26] Kodati P, Hinkle J, Winn A, Deng X. Microautonomous robotic ostraciiform (MARCO): hydrodynamics, design, and fabrication. IEEE Trans Robot 2008;24(1):105–17.
[27] Low KH, Chong CW. Parametric study of the swimming performance of a fish robot propelled by a flexible caudal fin. Bioinsp Biomim 2010;5:046002.
[28] Chen Z, Shatara S, Tan X. Modeling of biomimetic robotic fish propelled by an ionic polymer–metal composite caudal fin. IEEE/ASME Trans Mechatron 2010;15(3):448–59.
[29] Aureli M, Kopman V, Porfiri M. Free-locomotion of underwater vehicles actuated by ionic polymer metal composites. IEEE/ASME Trans Mechatron 2010;15(4):603–14.
[30] Yu J, Ding R, Yang Q, Tan M, Wang W, Zhang J. On a bio-inspired amphibious robot capable of multimodal motion. IEEE/ASME Trans Mechatron 2011;PP(99):1–10.
[31] Strefling PC, Hellum AM, Mukherjee R. Modeling, simulation, and performance of a synergistically propelled ichthyoid. IEEE/ASME Trans Mechatron 2012;17(1):36–45.
[32] Liu F, Lee K-M, Yang C-J. Hydrodynamics of an undulating fin for a wave-like locomotion system design. IEEE/ASME Trans Mechatron 2011;PP(99):1–9.
[33] Zhou C, Low KH. Design and locomotion control of a biomimetic underwater vehicle with fin propulsion. IEEE/ASME Trans Mechatron 2012;17(1):25–35.
[34] Marras S, Porfiri M. Fish and robots swimming together: attraction towards the robot demands biomimetic locomotion. J Roy Soc Interf 2012:1–13.
[35] Tan X. Autonomous robotic fish as mobile sensor platforms: challenges and potential solutions. Marine Technol Soc J 2011;45(4):31–40.
[36] Guo S, Fukuda T, Asaka K. A new type of fish-like underwater microrobot. IEEE/ASME Trans Mechatron 2003;8(1):136–41.
[37] Paquette JW, Kim KJ. Ionomeric electroactive polymer artificial muscle for naval applications. IEEE J Ocean Eng 2004;29(3):729–38.
[38] Kim B, Kim D, Jung J, Park J. A biomimetic undulatory tadpole robot using ionic polymer-metal composite actuators. Smart Mater Struct 2005;14:1579–85.
[39] Tao T, Liang Y-C, Taya M. Bio-inspired actuating system for swimming using shape memory alloy composites. Int J Automat Comput 2006;4:366–73.
[40] Tangorra J, Anquetil P, Fofonoff T, Chen A, Del Zio M, Hunter I. The application of conducting polymers to a biorobotic fin propulsor. Bioinsp Biomim 2007;2:S6–S17.
[41] Wiguna T, Heo S, Park HC, Goo NS. Design and experimental parameteric study of a fish robot actuated by piezoelectric actuators. J Intell Mater Syst Struct 2009;20:751–8.
[42] Zhang Y, Cong M, Guo D, Wang D. Design optimization of a bidirectional microswimming robot using giant magnetostrictive thin films. IEEE/ASME Trans Mechatron 2009;14(4):493–503.
[43] Valdastri P, Sinibaldi E, Caccavaro S, Tortora G, Menciassi A, Dario P. A novel magnetic actuation system for miniature swimming robots. IEEE Trans Robot 2011;27(4):769–79.
[44] Akhtar I, Mittal R, Lauder GV, Drucker E. Hydrodynamics of a biologically inspired tandem flapping foil configuration. Theor Comput Fluid Dyn 2007;21:155–70.
[45] Sfakiotakis M, Lane DM, Davies JBC. Review of fish swimming modes for aquatic locomotion. IEEE J Ocean Eng 1999;24(2):237–52.
[46] Harper KA, Berkemeier MD, Grace S. Modeling the dynamics of spring-driven oscillating-foil propulsion. IEEE J Ocean Eng 1998;23(3):285–96.
[47] Kelly SD. The mechanics and control of robotic locomotion with applications to aquatic vehicles. Ph.D. dissertation, California Institute of Technology; 1998.
[48] Kelly SD, Murray RM. Modelling efficient pisciform swimming for control. Int J Robust Nonlin Contr 2000;10:217–41.
[49] Mason R, Burdick JW. Experiments in carangiform robotic fish locomotion. In: Proceedings of the 2000 IEEE international conference on robotics & automation, San Francisco, CA; 2000. p. 428–35.
[50] Mason R. Fluid locomotion and trajectory planning for shape-changing robots. Ph.D. dissertation, California Institute of Technology; 2003.
[51] Kanso E, Marsden JE, Rowley CW, Melli-Huber JB. Locomotion of articulated bodies in a perfect fluid. Nonlin Sci 2005;15:255–89.
[52] Boyer F, Porez M, Leroyer A, Visonneau M. Fast dynamics of an eel-like robot c comparisons with Navier–Stokers simulations. IEEE Trans Robot 2008;24(6):1274–88.
[53] Or Y, Zhang S, Murray RM. Dynamics and stability of low-Reynolds-number swimming near a wall. SIAM J Appl Dynam Syst 2011;10(3):1013–41.
[54] McIsaac KA, Ostrowski JP. Motion planning for anguilliform locomotion. IEEE Trans Robot Autom 2003;19(4):637–52.
[55] Colgate JE, Lynch KM. Mechanics and control of swimming: a review. IEEE J Ocean Eng 2004;29(3):660–73.
[56] Guo J, Joeng Y-J. Guidance and control of a biomimetic autonomous underwater vehicle using body-fin propulsion. Proc Inst Mech Eng, Part M: J Eng Maritime Environ 2004;218:93–111.
[57] Saimek S, Li PY. Motion planning and control of a swimming machine. Int J Robot Res 2004;23(1):27–53.
[58] Melli JB, Rowley CW, Rufat DS. Motion planning for an articulated body in a perfect planar fluid. SIAM J Appl Dynam Syst 2006:650–69.
[59] Cochran J, Siranosian A, Ghods N, Krstic M. 3-D source seeking for underactuated vehicles without position measurement. IEEE Trans Robot 2009;25(1):117–29.
[60] Zhang Y-H, He J-H, Yang J, Zhang S-W. A computational fluid dynamics (CFD) analysis of an undulatory mechanical fin driven by shape memory alloy. Int J Automat Comput 2006;4:374–81.
[61] Anton M, Chen Z, Kruusmaa M, Tan X. Analytical and computational modeling of robotic fish propelled by soft actuation material-based active joints. In: Proceedings of the 2009 IEEE/RSJ international conference on intelligent robots and systems, St. Louis, MO; 2009. p. 2126–31.
[62] Tan X, Carpenter M, Thon J, Alequin-Ramos F. Analytical modeling and experimental studies of robotic fish turning. In: Proceedings of the IEEE international conference on robotics and automation, Anchorage, AK; 2010. p. 102–8.
[63] Chen H, Zhu C, Yin X, Xing X, Cheng G. Hydrodynamic analysis and simulation of a swimming bionic robot tuna. J Hydrodynam, Ser B 2009; 19(4):412–20.
[64] Wang J, Alequin-Ramos F, Tan X. Dynamic modeling of robotic fish and its experimental validation. In: Proceedings of the 2011 IEEE/RSJ international conference on intelligent robots and systems, San Francisco, CA; 2011. p. 588–94.
[65] Leonard NE, Graver JG. Model-based feedback control of autonomous underwater gliders. IEEE J Ocean Eng 2001;26(4):633–45.
[66] Bhatta P, Leonard NE. A Lyapunov function for vehicles with lift and drag: stability of gliding. In: Proceedings of the 43rd IEEE conference on decision and control, vol. 4; December 2004. p. 4101–6.
[67] Morgansen KA, Duindam V, Mason RJ, Burdick JW, Murray RM. Nonlinear control methods for planar carangiform robot fish locomotion. In: Proceedings of the 2001 IEEE international conference on robotics & automation, Seoul, Korea; 2001. p. 427–34.
[68] Fossen TI. Guidance and control of ocean vehicles. New York: Wiley; 1994.
[69] Arafat HN, Stilwell DJ, Neu WL. Development of a dynamic model of a small high-speed autonomous underwater vehicle. In: Proceedings of oceans, Boston, MA; 2006. p. 1–6.
[70] Yu J, Liu L, Wang L, Tan M, Xu D. Turning control of a multilink biomimetic robotic fish. IEEE Trans Robot 2008;24(1):201–6.
[71] Long Jr JH, Koob TJ, Irving K, Combie K, Engel V, et al. Biomimetic evolutionary analysis: testing the adaptive value of vertebrate tail stiffness in autonomous swimming robots. J Exp Biol 2006;209(23):4732–46.
[72] Tangorra JL, Lauder GV, Hunter IW, Mittal R, Madden PGA, Bozkurttas M. The effect of fin ray flexural rigidity on the propulsive forces generated by a biorobotic fish pectoral fin. J Exp Biol 2010;213:4043–54.
[73] Kanso E, Newton PK. Passive locomotion via normal-mode coupling in a submerged spring-mass system. J Fluid Mech 2009;641:205–15.